

# COMPUTATIONAL EVALUATION OF FLOW CONTROL FOR ENHANCED CONTROL AUTHORITY OF A VERTICAL TAIL

**Arvin Shmilovich, Yoram Yadlin and Edward Whalen**  
**The Boeing Company**

**Keywords:** *aerodynamics, CFD, Flow Control, tail*

## **Abstract**

*A computational method for predicting the aerodynamic performance of a vertical tail due to active flow control has been developed. Enhanced directional control using flow control technology can potentially result in reduced fuel burn and improved airplane performance. Results of the validation for various flow conditions, actuation parameters and port layouts using a representative vertical tail configuration are used to establish the accuracy of the numerical tool. A practical approach to facilitate preliminary evaluations of active flow control with quick computational turnaround is proposed. Aspects of integration into a vertical tail are presented and guidelines for preferred modes of actuation are put forth.*

## **1 Introduction**

The size of the vertical of a typical transport airplane is determined by the yawing moment required to maintain straight, stable flight. In particular, the vertical tail must provide sufficient control authority during a one-engine-inoperative (OEI) condition during takeoff. During an OEI event, one engine malfunctions such that operation of the remaining engine may induce rotation of the aircraft about the yaw axis in a direction towards the inoperative engine. This is especially critical for wing-mounted, twin engine aircraft, and particularly important with the advent of high thrust engines. For a given aircraft speed, the yaw control authority can be obtained with a sufficiently large vertical tail. However, large surface area is undesirable since it results in added weight and higher cruise drag, which increases fuel burn and

decreases aircraft performance. The required yaw control can be alternatively obtained by enhancing the side-force coefficient of the vertical tail. Recent experimental studies conducted by Rathay et al [1, 2] have demonstrated that Active Flow Control (AFC) can be used to augment the side-force coefficient of the vertical tail. This was achieved by placing an array of synthetic jet actuators (which produce pulsed blowing-suction flow) on the stabilizer and close to the rudder. The current study focuses on the development of a computational method for the aerodynamic assessment of a vertical tail that utilizes synthetic jet actuation. It is based on a numerical approach previously used to investigate actuation techniques for the control of separated flows, vortex systems and wing wakes [3-7]. The analysis procedure is extensively validated with the experimental data reported by Rathay et al [2] for a range of flow conditions and actuation modes, helping gain confidence in its use for the development of practical AFC solutions. Strategies for practical airframe integration are employed with the goal of providing guidelines for effective flow control implementations.

This paper will describe the computational approach in the framework of AFC, followed by validation with experimental data obtained for a tail model representative of a transport airplane. Various flow conditions, actuation parameters and port layouts are considered. The formal temporal accuracy of the numerical algorithm will be established for different actuation parameters. A practical simulation approach for estimating the incremental force due to pulse actuation is described and its validity is confirmed for a set of port layouts. Subsequent

analyses will demonstrate a systematic approach for devising AFC systems which are subject to a set of real world integration constraints.

## 2 Numerical Procedure

The numerical tool is a modified version of the OVERFLOW code originally developed by NASA [8] and it forms the core process of Boeing's transport aircraft CFD methodology. OVERFLOW is based on the unsteady Reynolds Averaged Navier-Stokes formulation for overset grid systems.

The numerical procedure has been modified by Shmilovich and Yadlin [3] in order to simulate flows for a family of flow control techniques. Special modules have been developed for the modeling of time-varying boundary conditions to simulate the flow excitation due to control devices. Jet actuation is described by the mass flow rate, cross sectional area and the stagnation pressure and temperature in order to define the velocity at the actuator nozzle. The numerical algorithm uses the characteristics approach for consistent application of the boundary conditions. In the case of pulsed jets the flux vector is aligned with the nozzle axis and jet pulsation is determined by the forcing frequency. Various signal shapes can be prescribed to represent the periodic efflux of the actuation devices.

In this study a second order upwind differencing scheme and the SA turbulence model have been used. Following the analysis of the accuracy of the numerical scheme in the framework of AFC that will be discussed in a subsequent section, the flow control computations use 800 time steps per actuation cycle. The calculation starts with a steady-state solution obtained for the flow in the absence of any actuation. Limit cycle convergence is usually achieved after approximately 100 actuation cycles.

## 3 Validation with Experimental Data

### 3.1 Geometrical Model

The numerical tool has been validated using a set of flow control experiments for various wing sections and a range of actuation modes [3, 5]. Here the validation is performed for a vertical tail model which has been extensively tested at the Rensselaer Polytechnic Institute [2]. Figure 1 shows the experimental model that consists of a vertical tail mounted on a rotating splitter plate, which allows for analysis at side-slip conditions with minimal interference from the tunnel wall boundary layer. A non-metric stub is placed between the rotating splitter plate and the wind tunnel wall. The actuators are installed on the suction side of the tail, i.e. on the side opposite to the rudder deflection. A set of 12 synthetic jet actuators are installed close to the trailing edge of the stabilizer. This effectively places the orifices of the actuators just upstream of the hinge line created by the rudder when it is being deflected. The tail cross section at a station that cuts through one of the orifices is shown in Figure 1, as well as the distribution of the four groups of 3-actuators each. The actuators are sequentially numbered, starting from the tip of the tail, so that the actuator closest to the mounting plate is the twelfth in the sequence. The notation for the individual actuator groups uses the following convention;

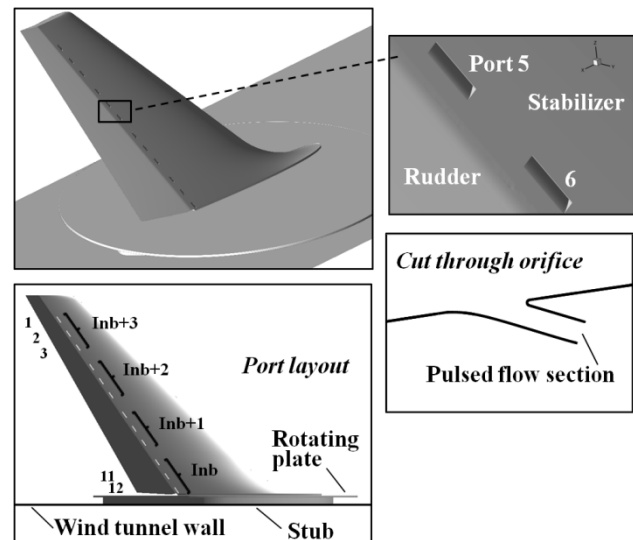
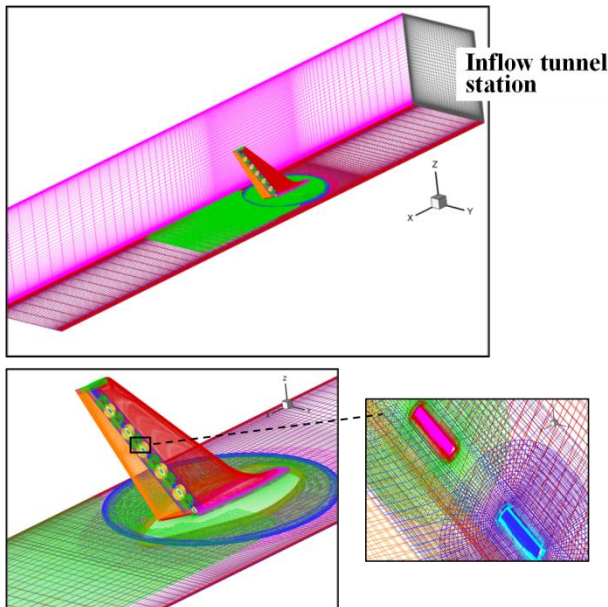


Fig. 1. Experimental tail model

the inboard group is denoted ‘Inb’, the adjacent group is ‘Inb+1’, and so on. For example, the group ‘Inb+2’ consists of actuators 4, 5 and 6. The actuators are placed with equal spacing within each group, and the groups are located at equal intervals along the tail.

### 3.2 Computational Setup

The computational domain consists of several overlapping grid systems that conform to all the solid surfaces, including the flow control ports. Figure 2 shows surface grids on the tail assembly, select tunnel walls and the tunnel inflow boundary. The grid consists of 23 million points and 56 sub grids.



**Fig. 2. Grid system**

Following the procedure described in Reference [3], the synthetic jet actuator is represented by an orifice having a constant cross sectional area and it is embedded within the tail. The orifice area and its orientation are consistent with the area and angle of the actuator at the exit station in the experimental setup. A set of fine sub grids are used for each orifice in order to resolve the interplay of the pulsed jet with the surrounding flow during the blowing and suction strokes.

The simulations are performed for a rudder deflected at a nominal angle,  $\delta_n$  representative

of a realistic flight condition. The solutions are obtained for a free stream velocity of 20 m/s which corresponds to a Mach number of 0.059. The mean chord Reynolds number is 0.35 million.

In the first step of the analysis the baseline flow without actuation is obtained using a steady state computation. The time-varying flow field is then obtained for the actuated flow. The pulsed actuation in the experiment is approximated at all the operating actuators with a sinusoidal signal having a frequency of 1600 Hz unless otherwise noted. A maximum jet velocity of 62.8 m/s is used, unless otherwise noted.

### 3.3 Side-slip Conditions

The first set of results is obtained for a set of progressively increasing side-slip angles, where  $\beta_1$  is the nominal case of zero degrees. Figure 3 shows the time-averaged surface pressure distributions on the suction side of the tail, the mounting plate and a portion of the wind tunnel wall. The flow fields include the flow separation bubbles (in gray surfaces), off-surface streamlines and the normalized total pressure,  $PT$ , at a cross sectional cut just downstream of the tail assembly. At these conditions the baseline flow fields (AFC off) in Figure 3a contain pockets of flow separation along the rudder, triggered by the adverse pressure gradient close to the hinge line. The flow off the rudder surface is in the general outboard direction. No separation occurs in the inboard segment of the rudder due to the edge effect as a result of the flow through the gap created by the deflected rudder and the rotating plate. At the higher side-slip conditions the pressure peaks at the leading edge of the tail in the outboard region result in slivers of separation bubbles which extend to the tip. Regions of separated flows also form in the front part of the rotating splitter plate due to its finite thickness, right-angle edge and in the wake of the stub.

The cross sectional cut depicts the wake profile which consists of the tail wake element and the bounded viscous layer at the side of the mounting wall. At increasingly higher side-slip angles the wake of the tail becomes thicker due

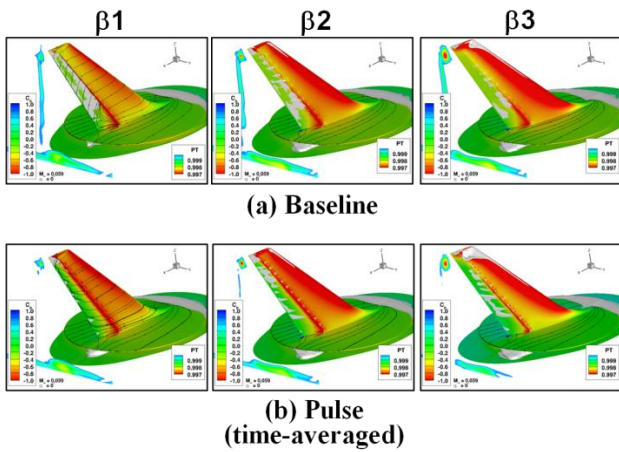


Fig. 3. Effect of 12-port actuation on the vertical tail

to the larger separation bubbles. The loss in total pressure also indicates that the trailing tip vortex gets stronger, commensurate with the increased tail loading at larger yaw.

The controlled flow fields (AFC on) are obtained with actuation having a peak velocity equivalent to about three times the free stream value. In terms of Mach number, the peak value is  $M_j=0.185$ . Flow control is applied at all ports with out-of-phase signals at adjacent ports. In other words, when the even number ports are at the peak of the blowing stroke, the odd number ports are at the point of maximum suction. The computed flow fields in Figure 3b indicate that in a time-average sense, the momentum imparted by the actuation generally provides more efficient flow turning along the rudder, which results in increased global circulation and higher side-force. At the side-slip of  $\beta_1$ , the all-port actuation results in the elimination of flow separation on nearly the entire span. The flow control is less efficient at the higher side-slip angles, where remnants of flow separation bubbles exist along the entire span of the rudder. The computed flow fields indicate that the intensity of the wakes is profoundly impacted by the actuation over the range of yaw conditions simulated.

The flow structure in the vicinity of port 5 is described next in Figure 4 for the  $\beta_1$  side-slip condition. The instantaneous and time-averaged flow features are shown in terms of iso-surfaces of the Mach number and the streamwise component of the velocity  $U_x$  at a spanwise station that cuts through the center of port 5. In

the limit cycle when a periodic flow has been reached, the net effect of the pulsed actuation is the addition of momentum into the flow whereby the time-averaged jets augment the Coanda effect over the rudder (compare Figures 4a and 4b). This flow mechanism is further described in Figure 4c at the instantaneous blowing and suction points of port 5. The actuation at the adjacent ports 4 and 6 displays an out-of-phase flow structure. In the blowing phase a packet of high velocity fluid is ejected from the orifice towards the rudder. The slug of high momentum travels over the rudder surface but it is rendered finite since the momentum supply ceases as the actuation reverts to the suction mode. In the suction phase the flow is by and large drawn into the actuator from the oncoming flow over the stabilizer.

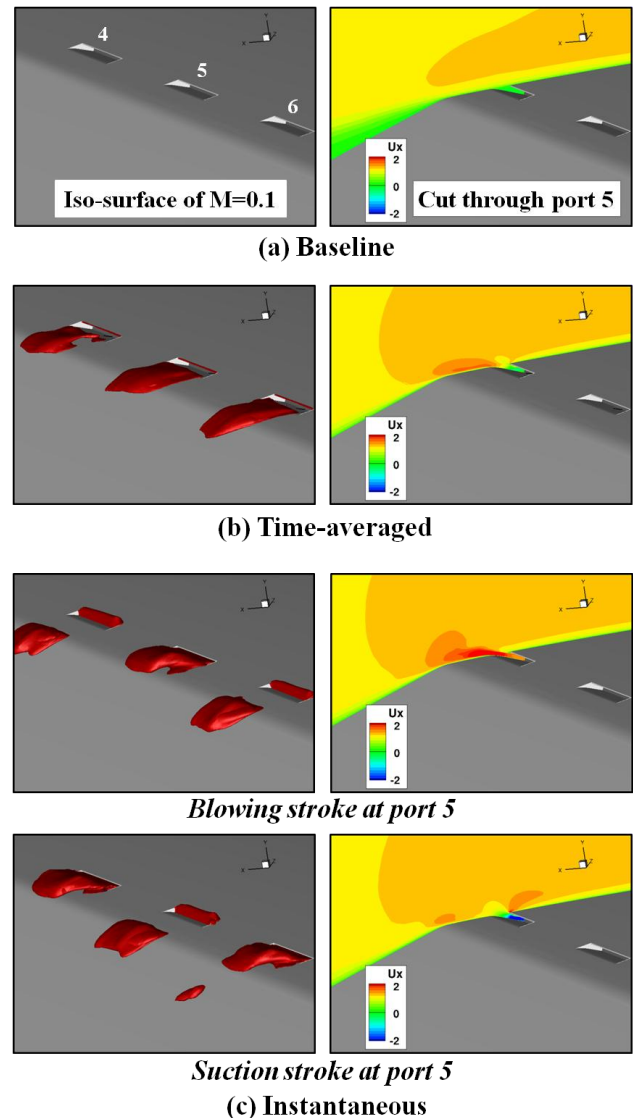
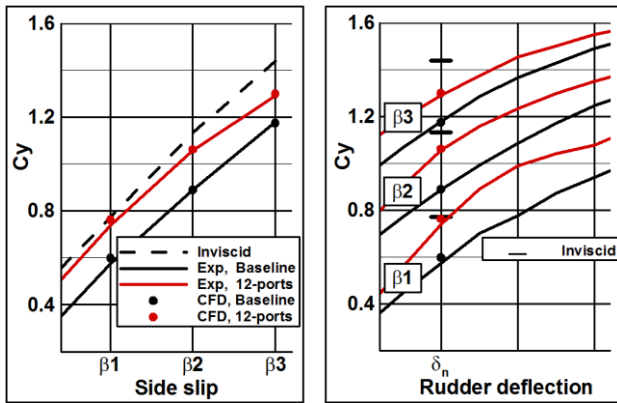


Fig. 4. Flow in the vicinity of port 5 at the  $\beta_1$  condition

## COMPUTATIONAL EVALUATION OF FLOW CONTROL FOR ENHANCED CONTROL AUTHORITY OF A VERTICAL TAIL

Comparisons with the measured data are presented in Figure 5, indicating reasonable agreement in terms of side-force coefficient  $C_y$  on the tail for a range of side-slip angles. The reduced flow control efficiency at larger side-slip conditions is evident in both the experimental observations and the computational results.



**Fig. 5. Side-force augmentation due to 12-port actuation**

In the analysis of AFC systems it is instructive to refer to the corresponding baseline inviscid flow [3]. The inviscid lift determines the theoretical upper limit of an airfoil to produce lift in the absence of viscous effects. Heuristically, AFC can be interpreted as the means to mitigate the viscous effects and achieve inviscid-like lift levels. Consequently, the inviscid lift level can be used as a yardstick for AFC efficiency. Throughout the following analysis, the inviscid lift (which is the side-force in this context) is used to gauge the performance of the various actuation patterns.

According to the predicted results in Figure 5, the actuation is quite effective at the nominal side-slip condition of  $\beta_1$ , where the side force is comparable to the inviscid level of the uncontrolled case. However, at higher side-slip angles the flow control is only partially able to alleviate the viscous effects, with notable degradation at large yaw.

Although the incremental force can be viewed as the figure of merit for the AFC tail application, the key to an efficient implementation requires further insight into the distribution of the load along the vertical tail. In view of the agreement with the measured data,

the computed flow fields are used to facilitate the diagnostics of the span load for a selected case from Figure 5. Figure 6 shows the span load and the sectional lift distributions for the  $\beta_1$  and  $\beta_3$  yaw angles. Here  $\eta$  denotes the normalized span coordinate, where  $\eta=0$  is the wind tunnel wall and 1 is the vertical tail tip. The curves span the distance between the rotating plate and a station close to the tip of the tail. The AFC port locations are indicated by the vertical grey bands.

Considering first the  $\beta_1$  case, the load distribution due to actuation closely resembles the inviscid flow, consistent with the side-force in Figure 5. The sectional force produces a peaky distribution in the outboard segment of the tail, indicative of critical tail sections where the flow is prone to separation. Indeed, at higher yaw angles the dip in the baseline distributions in the  $0.45 < \eta < 0.75$  range is indicative of the largest impact of flow separation on side-force. The flow control is quite effective in alleviating flow separation and increasing the side-force in that area. However, it is much less effective in the inboard portion, where the chord length is large and the flow separation is milder (see Figure 3a).

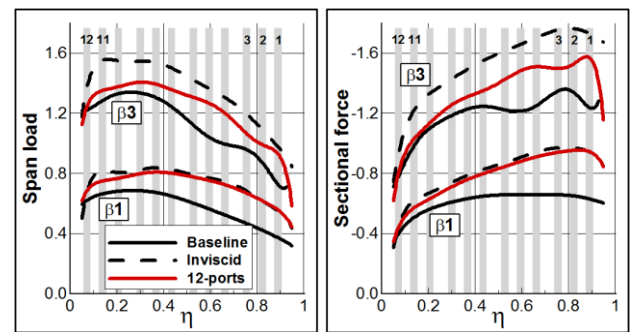


**Fig. 6. Predicted span load and sectional lift distributions**

### 3.4 Numerical Accuracy

The time-marching technique employs a second order Newton iterative process with sub-iterations. Although the method improves the robustness of the simulations for a range of actuation modes, it is important to establish the temporal accuracy of the numerical algorithm for this particular application. The results of this

analysis are presented in Figure 7 for the  $\beta_1$  side-slip case using different actuation levels. Pulsed actuation with peak Mach numbers of 0.185 and 0.37 are considered. The side-force is plotted as a function of the normalized time step ( $\Delta t$ ) to the  $n$ th power, where  $n$  is the assumed order of the numerical accuracy. Limit cycle solutions are obtained for a set of three time step values. Clearly the scheme is of second order in time and the temporal truncation errors are proportional to the actuation intensity. This is inferred from the slopes of the respective  $O(2)$  lines, where the higher slope of the  $M_j=0.37$  case is indicative of larger truncation errors.

Based on this analysis the finest time step was used for all the computations presented here (indicated by the arrow). It corresponds to 800 time steps per cycle for the 1600 Hz actuation. This choice strikes a practical balance between solution turnaround time and the temporal error. The magnitude of the error in the computed side-force can be easily estimated by visually extending the  $O(2)$  curves until they cross the vertical axis. The intersection points represent the theoretical side-force in the limit of vanishing truncation errors as  $\Delta t \rightarrow 0$ , i.e., the  $C_y$  that would have been obtained using infinitesimally small time steps. The expected error in the computed side-force is less than 1%, which is inferred from the difference between the respective computed and theoretical values.

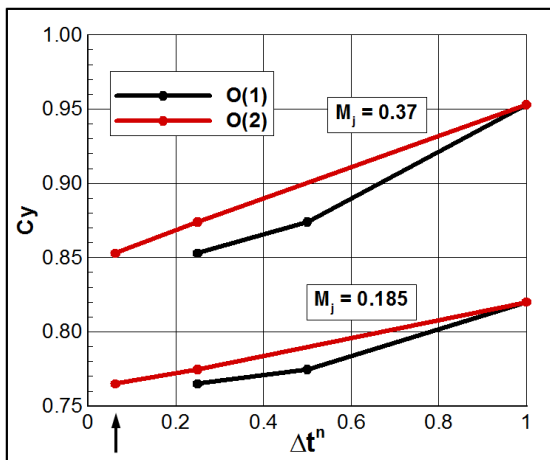


Fig. 7. Temporal accuracy of the numerical scheme

### 3.5 Port Actuation Patterns

Port placement is an important factor in the development of AFC systems. At this point it is instructive to validate the computational method for a family of actuation patterns, focusing on the span distribution of actuated ports. This will be accomplished through the specification of the boundary condition at the inlet station of the individual ports. In the first case only the even numbered ports are activated, i.e. ports 2, 4, 6, 8, 10 and 12. The non-operating ports are effectively stagnant flow cavities with no flow through. The second pattern employs actuation of the ports of group Inb+2 (ports 4, 5 and 6). The third scenario utilized actuation at port 5.

The computed flow fields at  $\beta_1$  are shown in Figure 8 and they should be compared to the corresponding baseline and all port actuation fields in Figure 3. The even port actuation results in an intermittent flow separation pattern on the rudder where pockets of reversed flow exist in the regions downstream of the unactuated ports. The Inb+2 actuation pattern helps reattach the flow locally over a region that covers about one quarter of the span. The actuation of the single number 5 port results in modest reduction in separated flow in its immediate vicinity.

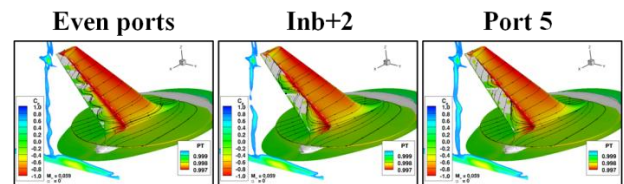
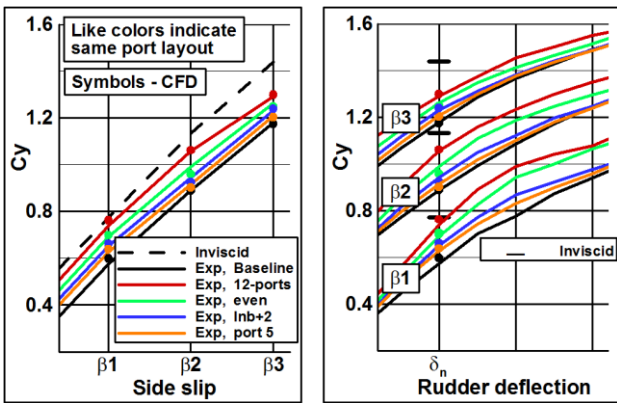


Fig. 8. Port actuation patterns at  $\beta_1$  (time-averaged)

The validation study of side-force augmentation due to the various flow control patterns is summarized in Figure 9. Here the experimental data is represented by the line curves and the computed values by the round symbols, where like colors denote similar actuation patterns. Consistent with the flow fields in Figures 3 and 8, the 12-port actuation provides the largest incremental force while the single port control results in modest gain. All the actuation patterns exhibit diminishing effectiveness at large yaw. The accompanying

**COMPUTATIONAL EVALUATION OF FLOW CONTROL FOR ENHANCED CONTROL AUTHORITY OF A VERTICAL TAIL**

spanwise distributions are shown in Figure 10. The uniform port distributions of the 12-port and even port patterns result in a global increase in span load over the entire element. On the other hand, the Inb+2 and port 5 actuation patterns produce localized load augmentation. The local actuation also increases the load in the adjacent outboard regions due to the prevailing spanwise component of the flow over the rudder surface.



**Fig. 9. Side-force due to various port layouts**

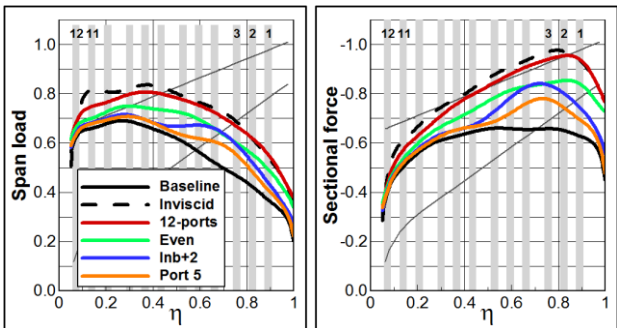


**Fig. 10. Span load distributions due to various port layouts at  $\beta_1$**

The computed side-force trends are generally in good agreement with the measured data. However, further examination of the incremental side-force due to AFC reveals notable discrepancies. This is shown in Figure 11 for various port patterns at the  $\beta_1$  side-slip, where the gain in side-force is plotted as function of number of actuated ports. The side-force gain per actuator, which is a measure of AFC efficiency, is also included in Figure 11. The computed results obtained with the sinusoidal actuation signal described in Section

3.2 are denoted by the blue symbols (connected by the blue line for convenience). It becomes apparent that the current computational model generally under predicts the side-force gains due to actuation. These discrepancies underscore the shortcoming in analyzing synthetic jet flows in the context of the current approach, i.e., the manner in which the boundary conditions are prescribed. The pulsed flow at the orifice is prescribed from data obtained from bench test experiments of an operating actuator. This data is determined from a set of hot wire measurements near the exit plane of the orifice and it constitutes an approximate representation of the flow. Often, this periodic flow is conveniently described by a sine wave. In this particular study, further inspection of the measured data revealed that a more adequate representation can be prescribed by a wave whose shape lies between a sine and a step function. Moreover, the blowing and suction waves are not identical in shape. Clearly, this represents a source of inconsistency with the AFC modeling. To assess the sensitivity to variations in the shapes of the forcing signal a series of solutions were obtained using an input signal that better represents the measured data. The results obtained in this fashion for the set of port patterns are included in Figure 11. Not surprisingly, the signal of the periodic excitation illustrates a certain level of variability in the predicted force levels. These numerical

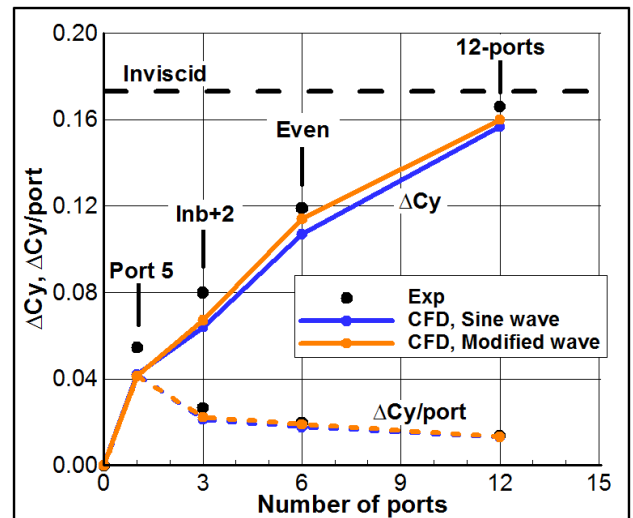


**Fig. 11. Side-force increments due to various port patterns at  $\beta_1$**

experiments indicate that the discrepancy with the experimental data is partly attributed to the inability to accurately prescribe boundary conditions to mimic realistic synthetic jets.

The results also show that the discrepancy with the measured data is more pronounced for the port layouts targeting localized separation control (Inb+2 and port 5). This is possibly due to the inability of the turbulence model to accurately capture the time-varying interaction of the pulsed jets with the surrounding separated flow. In contrast, solutions for higher port density cases where the separated flow on the rudder element is almost entirely eliminated produce forces in closer agreement with the experiment.

#### 4 Pulse Flow Analog

In the study of AFC it is very important to assess the effectiveness of different flow control modes. Although the focus of the current study is on synthetic jet actuation, it is instructive to compare its effect relative to a comparable constant blowing jet through the same port. Here the constant jet velocity is equivalent to the time-integrated velocity over both the blowing and suction strokes of the pulsed actuation. In the case of the sinusoidal wave with a peak of  $M_j=0.185$  the equivalent blowing jet Mach number is  $M_{j_{Bl}} = M_j \cdot (2/\pi)$ . This is described in Figure 12, where the negative Mach number signifies suction. Side-force comparisons between the pulsed flow actuation and the equivalent constant blowing for the set of actuation patterns are also presented,

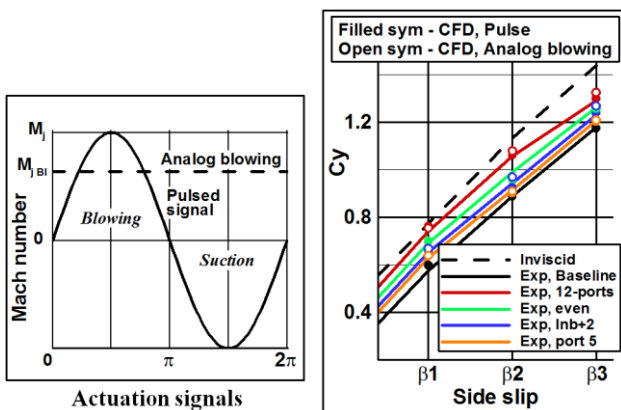


Fig. 12. Side-force obtained with the blowing analog

indicating fairly close agreement. Further examination of the flow fields indicates that the constant blowing actuation produces flow structures that closely resemble the respective time-averaged solutions obtained with pulsed actuation. Specifically, the flow fields shown in Figure 13a should be compared with those in Figure 3b for the all port actuation over the range of side-slip conditions. The flow fields in Figure 13b are the blowing analog counterparts of the pulsed jet actuation in Figure 8 for different actuation patterns. Also, the flow field obtained with the blowing analog in Figure 14 is quite similar to the synthetic jet time-averaged flow in Figure 4b. The similarity between the synthetic jet actuation and the blowing analog is also evident in the span load characteristics for the set of actuation patterns in Figure 15 and the accompanying side-force gains in Figure 16.

The evaluation study presented in Figures 12-16 demonstrates that the blowing analog is a useful approach for quickly obtaining flow fields that closely approximate time-averaged synthetic jet solutions.

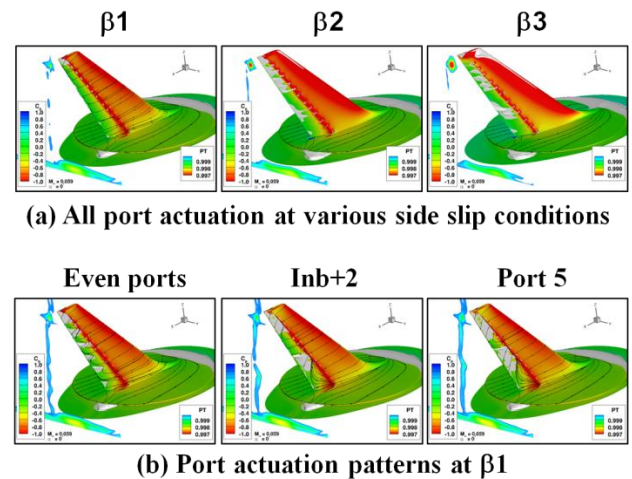


Fig. 13. Flow fields obtained with the blowing analog

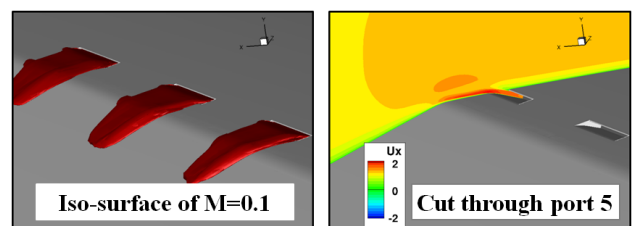
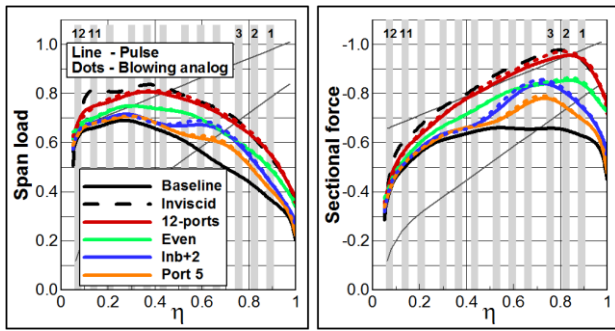
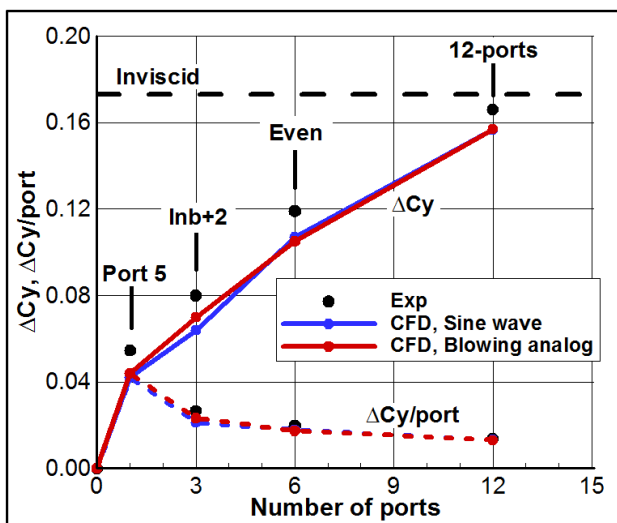


Fig. 14. Flow structure due to blowing analog at  $\beta_1$  (all port actuation)

## COMPUTATIONAL EVALUATION OF FLOW CONTROL FOR ENHANCED CONTROL AUTHORITY OF A VERTICAL TAIL



**Fig. 15. Comparison in span load distributions between pulsed actuation and blowing analog at  $\beta_1$**



**Fig. 16. Side-force increments due to the blowing analog at  $\beta_1$**

It isn't clear whether similar blowing analog approaches hold true for other synthetic jet type applications. If the blowing analog is deemed adequate, however, it is highly recommended to perform occasional spot checks to ascertain its range of validity.

### 5 Practical Considerations for AFC Layout

There is a set of factors that need to be carefully considered when implementing a flow control system. Obviously, input power required is a primary determinant of a practical integrated AFC system. Moreover, there are issues stemming from the altered aerodynamic characteristics that are important from an operational standpoint. The AFC lift increment along the span of the tail is an important design factor that needs to be addressed in this context.

For example, there are potential advantages to distributing the added AFC loads in the inboard tail segment for ease of integration (actuators being closer to power source in the fuselage), system packaging (availability of larger volume at the root of the tail), reduced roll moment during engine out operation (low roll rate into the inoperative engine) and improved aeroelasticity. These issues can be evaluated through computational analyses aimed at tailoring of the load using various port layouts and span varying actuation.

This point is illustrated next, with the focus on increased span load inboard while providing side-force for higher tail control authority. In this example two alternative actuation schemes are compared with the nominal 12-ports actuation. The 'Inb' (3 ports) and the combined 'Inb' and 'Inb+1' (6 ports) patterns are used with actuation intensity twice as large as the nominal actuation (denoted 2x) in order to attain the desired side-force. I.e., the actuation represents synthetic jets with an amplitude of  $M_j=0.37$ . The blowing analog will be utilized for quick solution turnaround. Figure 17 shows the results obtained with alternative actuation schemes at  $\beta_1$ , and compared with the nominal 12-port actuation in Figure 15. The results indicate that the actuation provides higher loads in the inboard segment with diminishing effects towards the tip of the tail. Also, a peaky sectional force distribution is usually a reliable indicator of the location at which flow separation ensues. Since the preferable location for separation onset is inboard, an aerodynamic benefit can be realized if the critical sections develop closer to the root of the tail. The inboard shift of the critical sections, from  $\eta=0.85$  to about  $\eta=0.45$ , obtained with the two port layouts is therefore advantageous. This is especially important at larger side-slip angles (not shown here).

The side-forces due to the inboard actuation patterns are shown in Figure 18. The augmentation provided by 'Inb' pattern is not sufficiently powerful to reach the performance of the nominal 12-port actuation. However, the combined 'Inb' and "Inb+1" actuation surpasses it, and provides side-force close to the inviscid level over the range of side-slip angles. This

mode of AFC implementation requires high power synthetic jet actuators capable of producing higher velocity, or equivalently, the same velocity through larger orifices.

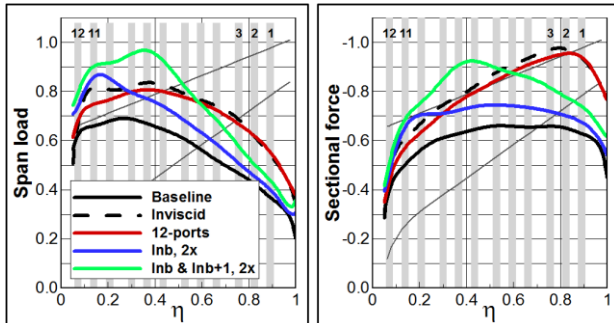


**Fig. 17. Aspects of integration have led to alternative inboard actuation with improved aerodynamic performance ( $\beta_1$  condition)**

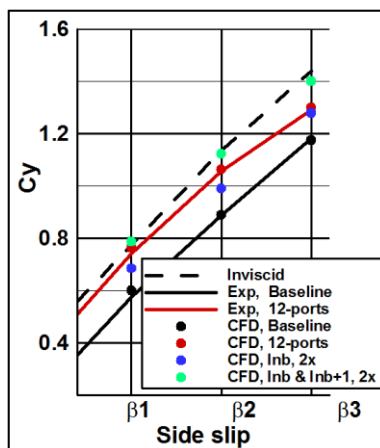


**Fig. 18. Side-force due to inboard actuation**

## 6 Conclusions

A computational procedure for the simulation of a synthetic jet actuation system on a vertical tail has been developed. Reasonable agreement with experimental data is obtained with well predicted trends across the practical range of side-slip conditions. Discrepancies are notable in cases of targeted application for control of flow separation at select span segments along the rudder, where smaller number of ports is used. A possible source of inconsistency is the deficiency of the turbulence model to accurately simulate time-varying interactive flows of pulsed jets and separated flows. Another

limitation in the current approach is the uncertainties in the experimental setup combined with the manner in which the boundary conditions are used to represent the synthetic jet flow.

A more direct approach to represent synthetic jet flows for consistent validation would require changes in both the measurement technique used to characterize the actuation and the computational model. Measurements tracking the displacement of the synthetic jet actuator diaphragm would be required to define the time dependent forcing applied to the flow in an unambiguous manner. This information would then be used to define the flexing of the diaphragm in the numerical procedure, utilizing a moving boundary procedure. The computational domain would include the complete flow field, consisting of the external flow as well as the actuator chambers of the individual ports. Obviously, this approach would represent a higher level of computational complexity in the framework of simulating flow control using synthetic jets.

The investigation of AFC for the vertical tail demonstrates that constant actuation can be used as proxy for predicting the effects of the unsteady actuation from synthetic jets. This is a useful tool which facilitates quick analyses and helps draw guidelines for preferred synthesis into flight platforms in the early stages of the design cycle.

## References

- [1] Rathay N W, Boucher M J, Amitay M and Whalen E. Performance enhancement of a vertical tail using synthetic jet actuators. AIAA Paper 2012-71.
- [2] Rathay N W, Boucher M J, Amitay M and Whalen E. Performance enhancement of a vertical stabilizer using synthetic jet actuators: non-zero sideslip. AIAA Paper 2012-2657.
- [3] Shmilovich A and Yadlin Y. Flow control for the systematic buildup of high lift systems. Journal of Aircraft, Vol. 45, No. 5, pp 1680-1688, 2008.
- [4] Shmilovich A and Yadlin Y. Active flow control for practical high-lift systems. Journal of Aircraft, Vol. 46, No.4, pp 1354-1364, 2009.
- [5] Khodadoust A and Shmilovich A. High Reynolds numbers simulations of distributed Active Flow Control for a high-lift system. AIAA Paper 2007-4423.

## COMPUTATIONAL EVALUATION OF FLOW CONTROL FOR ENHANCED CONTROL AUTHORITY OF A VERTICAL TAIL

- [6] Yadlin Y and Shmilovich A. Computational method for assessment of flow control techniques for airplane propulsion systems. AIAA Paper 2008-4084.
- [7] Shmilovich A and Yadlin Y. Flow control techniques for transport aircraft. AIAA Journal, Vol. 49, No 3, pp 489-502, 2011.
- [8] Buning P G, Chiu I T, Obayash S, Rizk Y M and Steger J L. Numerical simulation of the integrated space shuttle vehicle in ascent. AIAA Paper 1988-4359.

### 7 Contact Author Email Address

arvin.shmilovich@boeing.com

### Copyright Statement

The authors confirm that they, and/or their company or organization, hold copyright on all of the original material included in this paper. The authors also confirm that they have obtained permission, from the copyright holder of any third party material included in this paper, to publish it as part of their paper. The authors confirm that they give permission, or have obtained permission from the copyright holder of this paper, for the publication and distribution of this paper as part of the ICAS 2014 proceedings or as individual off-prints from the proceedings.